Structural, electronic, and magnetic properties of thin Mn/Cu(100) films

M. Eder, J. Hafner, and E. G. Moroni
Institut für Materialphysik and Center for Computational Materials Science, Universität Wien, A-1090 Wien, Austria
(Received 31 August 1999; revised manuscript received 11 November 1999)

The atomic structure, electronic, and magnetic properties of thin Mn films epitaxially grown on Cu(100) substrates have been investigated by *ab initio* density-functional studies. Because the local-density approximation leads to a rather poor description of the magnetostructural properties of bulk Mn, a detailed study of the effect of generalized gradient corrections (GGC) to the exchange-correlation functional on the structure and magnetism of Mn in three and two dimensions has been performed. For the bulk we find that the GGC's lift the almost-degeneracy between the competing magnetic configurations and lead to a large magnetovolume effect, in much better agreement with experiment. For free-standing Mn monolayers the effect of the GGC's is even more pronounced: the relative stability of square and hexagonal layers is inverted, antiferromagnetic ordering leads to a large increase of the equilibrium distances. Therefore all investigations of Mn films on Cu substrates have been performed in the generalized gradient approximation. The results demonstrate that homogeneous Mn overlayers are unstable against interdiffusion and the formation of ordered surface alloys. At a coverage of $\Theta = 0.5$ Mn monolayers, an ordered ferromagnetic $c(2\times2)$ surface alloy is formed. The same atomic structure is assumed at a coverage of $\Theta = 1$ and leads to an antiferromagnetic coupling between the CuMn alloy layers. In both homogeneous alloy layers and in the surface alloys, Mn is in a high-spin state with a magnetic moment close to $4\mu_B$. The large atomic volume of magnetic Mn leads an outward relaxation of the Mn atoms and a pronounced buckling of the surface. Detailed comparisons of the calculated atomic structure with low-energy electron diffraction and photoelectron diffraction experiments and of the electronic structure with photoemission and inverse photoemission spectroscopies are reported.

I. INTRODUCTION

One of the basic predictions of the theoretical studies of transition-metal magnetism is the increase of the magnetic moment at expanded volume. From this point of view, Mn is a particularly interesting case because according to Hund's rule the magnetic moment of the free atom is as large as $5\mu_B$. Mn is also known to form strongly ferromagnetic compounds such as MnSb,[1] and to have a magnetic moment of $4.9\mu_B$ as a dilute impurity in Cu.[2] If such a large magnetic moment (or even something close to it) could be stabilized in a ferromagnetic lattice, this would constitute a major advance in atomically engineered magnetic materials. A large number of theoretical studies has been devoted to the magnetic properties of the various crystalline phases of Mn.[3–13] Local spin-density theory predicts a rather small equilibrium volume of about 10 Å^3/atom for the face-centred-cubic (fcc, γ-Mn), body-centred-cubic (bcc, δ-Mn), and the hexagonal-close-packed (hcp, ϵ) phases of Mn. Fcc-Mn has an antiferromagnetic low-spin ground state, bcc-Mn is predicted to be paramagnetic, and hcp-Mn is in an antiferromagnetic low-spin-state. A transition to a high-spin state occurs only at an expansion of about 20%. At an atomic volume of $\sim$12 Å^3, the magnetic moment of fcc-Mn reaches a value of $\sim 2\mu_B$ which is comparable to the zero-temperature extrapolation of the magnetic moment of quenched γ-Mn ($m = 2.3\mu_B$, see Ref. 14). The problem is the experimental realization of a situation in which Mn assumes such a large atomic volume. Recent results indicate, however, that local spin-density theory might yield only a rather poor description of the magnetostructural properties of Mn (quite as it fails to predict the correct magnetic ground state for iron [10,11]). Nonlocal corrections to the exchange-correlation functional in the form of a generalized gradient approximation (GGA) lift the energetic almost-degeneracy of the competing magnetic phases and predict a substantially larger equilibrium volume for the antiferromagnetic than for the paramagnetic states of both γ- and δ-Mn. However, the linear muffin-tin orbital (LMTO) calculations performed in the GGA predict antiferromagnetic hcp ϵ-Mn to be more stable than the fcc γ phase. Therefore we return to the problem of the structural and magnetic energy differences of the various phases of Mn in order to test the reliability of the ultrasoft pseudopotential approach.

Thin Mn films have been grown on a number of fcc [Al,[15] Cu, Ni,[16] Ru, Ni,[17] Pd,[18] Ir (Ref. 19)] and bcc [Fe (Refs. 17 and 20)] substrates oriented in the (001) direction. In each case the Mn overlayers continue the square lattice of the substrate and adopt a nonuniformly strained fcc [face-centred-tetragonal (fct) or equivalently body-centred-tetragonal (bct)] structure. A volume increase of up to 10% compared to γ-Mn is reached and in all cases an antiferromagnetic behavior was observed. Hence the growth of thin Mn layers on suitably chosen substrates represents a possibility to realize the high-volume–high-spin state of Mn suggested by the local spin-density (LSD) calculations. Theoretical studies[21–24] and experiments agree on in-plane $c(2\times2)$ antiferromagnetism in the monolayer limit and layered antiferromagnetism for films with two and more monolayers.

The investigation of the structure and growth of thin Mn films on Cu(100) substrates by Flores, Hansen, and Wuttig[25] using Auger electron spectroscopy (AES) and low-energy electron-diffraction (LEED) techniques illustrates the strong dependence of the properties of the films on the growth conditions. At growth temperatures below 270 K, Mn grows in a

$c(8\times2)$ structure up to about monolayer coverage and rearranges in a $c(12\times8)$ structure at higher coverage. Above 270 K, Mn is incorporated into the surface, forming ordered surface alloys with a $c(2\times2)$ structure. The low-temperature structures undergo irreversible phase transitions on annealing, demonstrating that the surface alloy is the thermodynamically stable phase. The formation of a 50/50 surface alloy is remarkable because in the bulk solid solubility is restricted to much lower Mn contents and no stable CuMn intermetallic phase is known to exist. The CuMn surface alloy also shows remarkable magnetic properties. Short- and long-range spin-polarization effects of $c(2\times2)$ Mn/Cu(001) have been studied by O'Brien and Tonner.[26] They found that Mn is in a high-spin ground state, which stabilizes the surface reconstruction, but that long-range magnetic ordering is not always present. The electronic structure of (supposedly pure) Mn overlayers on Cu(100) has been studied by Binns and Norris[28] by AES and ultraviolet photoelectron spectroscopy (UPS). Inverse photoelectron spectroscopy (IPES) has been used by Hayden, Pervan, and Woodruff[27] to explore the atomiclike high-spin ground state of Mn atoms in the surface layer. Rader *et al.*[29] have used both angle-resolved ultraviolet photoemission (ARUPS) and IPES to characterize the electronic properties of the well-ordered $c(2\times2)$ CuMn surface alloys. The stability of the two-dimensional ordered CuMn surface alloy has been studied by Wuttig, Gauthier, and Blügel [30] using low-energy electron-diffraction (LEED) analysis and by *ab initio* local density-functional methods, identifying the high-spin state of Mn as the driving force behind the correlated large buckling and the stability of the surface alloy. However, a substantial difference exists between the exchange splitting derived from the combined UPS/IPES data and the theoretical predictions.

In our present paper we return to the problem of the description of the structural, electronic, and magnetic properties of Mn overlayers on Cu(100) substrates. In view of the result that the magnetic properties of pure Mn are correctly described only when a gradient corrected exchange-correlation functional is used, our investigations are based on the generalized gradient approximation. The organization of the article is as follows. In Sec. II we present briefly the main features of the computational method and of the construction of ultrasoft pseudopotentials (USPP) for magnetic Mn. The transferability and accuracy of Mn USPP in the context of spin-polarized solid phases and monolayers is described in Sec. III. The USPP results are compared with available full potential and experimental data. The GGA calculations describe better the stability and magnetic properties of bulk and monolayers and are used for the subsequent studies of Mn and CuMn films on Cu(100). Section IV describes the structural and magnetic properties of Mn/Cu(100) overlayers while Sec. V resumes the properties of CuMn/Cu(100) surface alloys. Both 1 monolayer (ML) and 2 ML's have been investigated. In Sec. VI the results are summarized and compared with available experimental data. Section VII contains our conclusions.

II. COMPUTATIONAL METHOD

Our study is based on density-functional theory,[31] using both the local spin-density approximation (LSDA) with the exchange-correlation functional proposed by Perdew and Zunger[32] and the generalized gradient approximation (GGA) in the form of Perdew *et al.*[33,34] For intermediate spin polarizations the interpolations formula of von Barth and Hedin[35] are applied. The approach of White and Bird[36] has been extended to compute the GGA spin-polarized exchange-correlation potentials.[37]

The calculations are performed in a plane-wave basis, using the Vienna *ab initio* simulation program VASP.[38–40] Within VASP, the electron-ion interactions are described by ultrasoft Vanderbilt-type pseudopotentials.[41,42,37] VASP uses iterative strategies for the calculation of the eigenvalues and eigenvectors of the generalized Kohn-Sham Hamiltonian for USPP, based on the minimization of the norm of the residual vector to each eigenstate[39,43] and preconditioned conjugate gradient techniques. Broyden[44] and Pulay[45] strategies for charge-density mixing are used to accelerate convergence of charge and spin densities and potentials.

Brillouin-zone integrations are performed on a grid of Monkhorst-Pack special points.[46] The linear tetrahedron method including the corrections of Blöchl[47] has been chosen to improve the convergence of the electronic structure and total energy with respect to the number of k points. The partial (site- and angular-momentum decomposed) spin-polarized densities of states are calculated in terms of a projection of the plane-wave components of the eigenstates onto spherical waves inside each atomic sphere.[48]

A. Ultrasoft pseudopotential

Ultrasoft pseudopotentials for Mn and Cu have been generated, respectively, in the nonmagnetic $4s^1 3d^6$ and $4s^1 3d^{10}$ atomic configurations, with cutoff radii of 2.2, 2.5, 2.5 a.u. for the $4s$, $4p$, and $3d$ components. All these pseudowave functions have strictly no node and very good scattering properties. By choosing two projectors at two different energies around each bound state, the logarithmic derivatives are very accurate over a wide range of energies not only for the $l=0-2$ components, but also for the unoccupied l=3 orbitals (f states). The local potential equals exactly the screened all-electron potential for $r>1.7$ a.u., while inside the core region it has the form $C\sin(Ar)/r$. C and A are determined such that the potential is continuous at the cutoff radius. With this setup, a low cutoff energy of $E_{cut}=230$ eV can be used for describing the US pseudowave function for Cu and Mn. A larger cutoff of $E_{cut}=390$ eV is required to describe the augmentation functions.

For both $3d$ metals, the nonlinear partial core correction scheme proposed by Louie, Froyen, and Cohen[49] has been used to describe the valence-core interaction. Pseudopotentials used in LSDA and GGA calculation of bulk or film properties have been generated from LSDA and GGA calculations for the chosen atomic reference configuration. For more specific details concerning the generation of ultrasoft pseudopotentials we refer to Ref. 42, concerning the specificities of using pseudopotentials for magnetic elements; see Ref. 37. In the following section we discuss the accuracy and transferability of the USPP for Mn in the context of spin-polarized bulk and monolayer calculations.

B. Slab geometry and convergence of calculation

1. Monolayer

For a free-standing Mn monolayer (ML) we have studied the nonmagnetic (NM) and ferromagnetic (FM) ordered $p(1\times1)$ and the antiferromagnetic (AF) $c(2\times2)$ phases for both square and hexagonal lattices, i.e., for atomic geometries corresponding to the (100) and (111) surfaces of fcc Mn. The Brillouin-zone integrations for the monolayers have been performed using different Monkhorst-Pack grids of about 40 to 70 special k points for the square and hexagonal layer, respectively. Using 42 k points corresponding to a $(11\times11\times3)$ grid insures that all total energies and local moments are converged to within 5 meV/atom and $0.01\mu_B$, respectively. The monolayer calculations are also well converged with respect to the width of the vacuum layer separating the repeated slabs; the present calculations are performed for a vacuum corresponding to eight atomic layers, the error in the total energy resulting from interactions across the vacuum is estimated to be below 5 meV/atom. The energy cutoff is the same as in the bulk calculations.

2. Overlayers and surface alloy

For the Mn overlayer and surface-alloy calculations we have used only the GGA. Smearing methods based on finite-temperature local density functional theory[50] with Methfessel and Paxton[51] broadening function are used for all surface and overlayer calculations. The optimized surface and overlayer geometries are determined by computing the Hellmann-Feynman forces acting on atoms and using conjugate gradient techniques to minimize the total energy.

Most of the calculations for the Mn overlayers or CuMn alloy films on Cu substrate are performed for $p(1\times1)$ FM, NM, and layered AF and $c(2\times2)$ in-plane AF configurations. The geometry and the input parameters concerning the magnetic and structural degrees of freedom for each supercell are presented below. The calculated GGA equilibrium lattice constant of fcc Cu ($a_0=3.643$ Å) has been used to fix the coordinates of the ''bulk layers'' in our slab calculations. This value is slightly larger than the experimental value of $a_0=3.614$ Å.

The convergence of the total energy for the film plus substrate complex has been tested with respect to (i) the number of surface layers being allowed to relax, (ii) the thickness of the vacuum layer, and (iii) the number of k points. As a first example, we refer to the convergence test for the buckling Δz of the alloy monolayer in the 1-ML CuMn/Cu(100) system versus the number of Cu substrate layers and versus the k-point sampling. Δz seems not to depend critically on the number of substrate layers. In fact, for the 1-ML CuMn/Cu(100) slab characterized by six Cu substrate layers and $(8\times8\times1)$ or $(9\times9\times1)$ Monkhorst-Pack grids, we obtain the same $\Delta z=0.26$ Å as when using a slab with ten substrate layers and a $(6\times6\times1)$ k-point grid. As second example, we discuss the magnetic energy difference between NM, FM, and AF configurations of 2-ML Mn/Cu(100). Exactly the same energy differences of $E_{FM}-E_{NM}=-0.42$ eV/Mn atom and $E_{AF}-E_{NM}=-0.55$ eV/Mn atom are obtained for six substrate layers and a $(16\times16\times1)$ grid and for ten substrate layers and a $(12\times12\times1)$ grid.

III. MAGNETISM OF MN IN THREE AND TWO DIMENSIONS: THE IMPORTANCE OF GENERALIZED GRADIENT CORRECTIONS

In this section we study the the accuracy of ultrasoft pseudopotentials and the influence of generalized gradient corrections on the prediction of structural and magnetic properties in the context of calculations for the different crystalline phases and for free-standing monolayers. The analysis of our results for the structural stability and magnetic properties of NM, FM, and AF states of fcc, hcp, and bcc Mn using the ultrasoft pseudopotential method illustrate both the accuracy of the pseudopotential approach and the importance of the GGA corrections. For both bulk crystals and monolayers we find that LSDA and GGA predict different structural and magnetic ground states.

A. fcc, hcp, and bcc Mn

For each structure (fcc, hcp, and bcc) and magnetic phase (NM, FM, and AF), the total energy and local moments are computed as a function of volume. The position of the minimum in the energy vs volume curve gives the equilibrium lattice constant and the curvature at the minimum is related to the bulk modulus at equilibrium. The ground-state properties have been obtained from a least-square fit of the total energies computed at a series of fixed volumes to a Murnaghan equation of state.[52] Approximately 100 k points in the irreducible wedge of the Brillouin zone (IBZ) per atom in the unit cell are required to converge the relative total energy within 1 meV/atom. To facilitate the calculation of energy differences between various structural and magnetic configurations, we have chosen whenever possible the same bct unit cell (as for AF also for FM and NM) and used a grid of 126 k points in the IBZ.

1. Structural and magnetic energy differences—LSDA results

The total energies and local magnetic moments of the FM, AF, and NM states of bcc, fcc, and hcp Mn as a function of the atomic volume calculated in the LSDA are compiled in Fig. 1. The antiferromagnetic structures of type AF1 and AF2 can be regarded as layered AF superlattices of period $p=1$ and orientation $G=(100)$ and $G=(111)$ of the planes containing parallel moments. Our USPP calculations agree reasonably well with LMTO (Refs. 10 and 11) results and are in excellent agreement with full potential (FP) LMTO (Ref. 13) total-energy calculations which both indicate the NM hcp phase as the most stable. For the equilibrium atomic volume V_0, all NM phases range between 10.08 and 10.16 Å^3, corresponding to an equilibrium Wigner-Seitz radius $r_{WS}\approx2.53$ a.u. For the same quantities, the FP LMTO result[13] is $r_{WS}\approx2.53$ a.u., while the LMTO result[10,11] gives $r_{WS}\approx2.59$ a.u.

Among the three structures considered here the NM hcp phase has the lowest energy and the structural energy difference between the NM hcp and fcc phases is only 3 mRy/atom using USPP, 4 mRy/atom using FP LMTO and 6 mRy/atom using LMTO. The energy difference between the NM hcp and bcc phases is about a factor of 3 larger, magnetic energy differences are even smaller than structural energy differences. Energetically almost degenerate AF1 and AF2

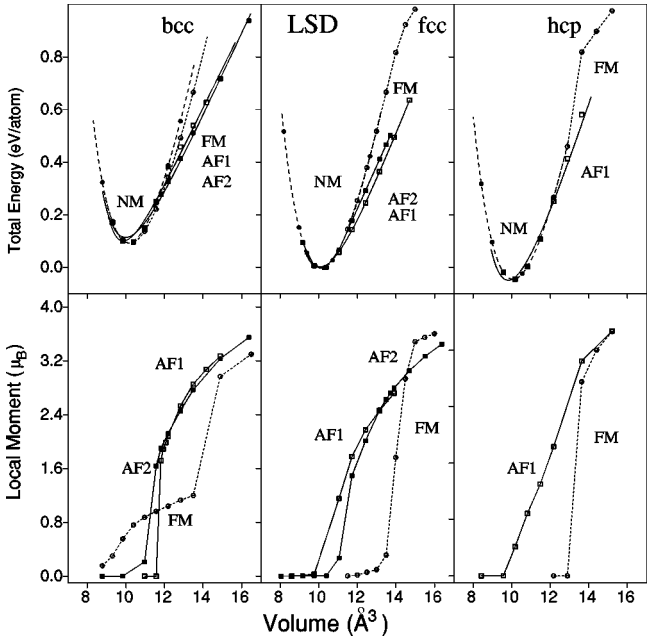

FIG. 1. Total energy and magnetic moment as a function of volume for the NM (full circles), FM (open cirles), AF1 (open box), and AF2 (full box) phases of bcc, fcc, and hcp Mn calculated in the LSDA. The energy is given relative to the AF1 fcc ground state.

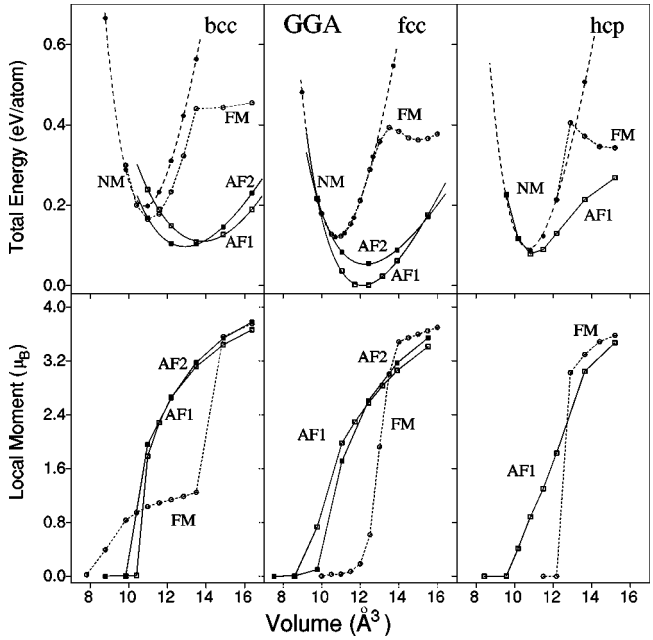

FIG. 2. Total energy and magnetic moment as a function of volume for the NM (full circles), FM (open cirles), AF1 (open box), and AF2 (full box) phases of bcc, fcc, and hcp Mn calculated in the GGA. The energy is given relative to the AF1 fcc ground state.

solutions are found for both fcc and bcc Mn, but in all cases AF solutions exist only at a slightly expanded volume. We also predict for FM bcc Mn a relatively small moment in the volume range of 9 to 14 Å^3, and a large moment in the region $V>14$ Å^3. This low-spin/high-spin transition for FM bcc Mn occurring at about $r_{WS}\approx 2.8$ a.u. compares very well with previous investigation of Fuster *et al.*[4] All these results indicate an excellent agreement between USPP and all-electron calculations. However, when compared with experimental results, the LSDA gives too small equilibrium volumes and cannot predict an AF ordering for the ground state of fcc Mn.

2. Structural and magnetic energy differences—GGA results

Figure 2 shows the same total energy and magnetic results as in Fig. 1, but now calculated using the GGA. The comparison of the two figures demonstrates that the gradient corrections lift the energetic degeneracy of the different magnetic phases and lead to strong magnetovolume effects. In agreement with previous studies[10,11,37,53–55] we find that the GGA increases the calculated equilibrium volumes, and reduces the bulk moduli. These effects are more pronounced in the magnetic phases, in agreement with earlier results on Fe.[37] As in Fe, we find in Mn that the FM phases have a larger equilibrium volume than either the AF or NM phases. The origin of the magnetovolume effect is in the occupation of antibonding orbitals of the majority spins and the depletion of the bonding states of the minority spins. However, in contrast to Fe, AF ordering leads to a stronger reduction of the total energy than FM ordering. The ground state is now the AF1 fcc phase, AF ordering is also preferred in the other two structures, although only a very small magnetic energy difference is predicted between NM and AF hcp Mn. As can be seen in Fig. 2, $\Delta V=V_{GGA}-V_{LSDA}$ is larger in bcc Mn for the AF1 than for the AF2 phase, and vice versa for the AF1 and AF2 phases in fcc Mn. The stabilization of the AF fcc phase arises almost entirely from the gain in magnetic energy, while the structural energy differences between the paramagnetic phases are very little influenced by the nonlocal corrections. The magnetic energy gain for both AF1 and AF2 depend sensitively on the given crystal structure. A crossover of the AF1 and AF2 total energies is found via uniaxial deformation along a Bain path connecting fcc and bcc Mn, for V_0 ranging from 12 to 14 Å^3.

Table I summarizes the computed LSDA and GGA ground state and magnetic properties. The AF1 configuration is stable for both fcc and hcp Mn while AF2 is favored in bcc Mn. In contrast to the LMTO results of Asada and Terakura,[10,11] which predict AF hcp Mn as ground state, the lowest energy is obtained for AF1 fcc Mn with the USPP method. Moreover, for bcc Mn we found as ground state the AF2 configuration and not the low-spin FM configuration as found by using LMTO. The difference in the fcc-hcp relative stability is probably related to the neglect of nonspherical contributions in the atomic-sphere approximation of the LMTO method which may play an important role because of different interstitial charge densities of Mn atoms for the various structure and magnetic states. Finally, using USPP our magnetic moment calculated for the AF fcc phase at $T=0$ K ($m_0\approx 2.4\mu_B$) is in good agreement with the magnetic moments estimated by extrapolating the experimental high-temperature data to room temperature ($m_0\approx 2.3\mu_B$ according to Refs. 14 and 57–59). In summary we can conclude that the GGA leads to a very much improved description of the structural and magnetic properties of Mn compared to the LSDA. Current work[56] extends these studies to the more complex α and β phases and definitely seems to confirm the superiority of the GGA.

TABLE I. Structural, cohesive, and magnetic properties of the energetically most favorable magnetic phases of fcc, bcc, and hcp Mn calculated in the LSDA and GGA. ΔE_s is the total-energy difference with respect to the AF1 fcc phase, V_0 the atomic equilibrium volume, a_0 the equilibrium lattice constant, B_0 the bulk modulus, and m_0 is the magnetic moment.

	Structure	Phase	ΔE_s (eV/atom)	V_0 (Å^3/atom)	a_0 (Å)	B_0 (Mbar)	$\lvert m_0\rvert$ (μ_B)
	bcc	NM	0.13	10.16	2.729	3.10	0.0
LSDA	hcp	NM	−0.04	10.08	2.425	3.13	0.0
	fcc	NM	0.00	10.12	3.433	3.10	0.0
	bcc	AF2	0.10	12.90	2.955	0.63	2.9
GGA	bcc	AF1	0.12	13.80	3.022	0.60	3.2
	hcp	AF1	0.10	11.08	2.502	1.00	0.8
	fcc	AF1	0.00	12.19	3.653	0.95	2.4
Expt. [a]	fcc	AF1		12.94			2.3

[a]Values obtained by extrapolation of high-temperature data to room temperature. After Ref. 57.

B. Body-centered-tetragonal Mn: Variation of energy and magnetic moments imposed by epitaxial constraints

Due to the size mismatch and the tendency to preserve the local atomic volume, fcc Mn films grown on Cu(100) substrates will be tetragonally strained. Due to the large magnetovolume effect in Mn, the size mismatch and hence the strain in the overlayer will depend on its magnetic state. By using *ab initio* calculations we have access to strain energy and local moment changes imposed by the epitaxial constraint. In Fig. 3 we compare the dependence of GGA total energy and of the magnetic moment of the NM, FM, and AF states of body-centered-tetragonal (bct) Mn on the axial ratio c/a, with the lateral lattice constant constrained to match Cu(100) surface. Because of the similar nearest-neighbor distance on the Cu(100) surface ($a_0=2.576$ Å) and in fcc AF1 Mn ($a_0=2.578$ Å) the total energy is minimized at $c/a=1.39$. This c/a ratio is only 1.7% smaller than the ideal fcc value of $c/a=\sqrt{2}$. This small contraction is not only related to the very small misfit strain but displays also a magnetically induced tetragonal lattice distortion of fcc AF Mn. This distortion has been explained by Oguchi and Freeman[60] in terms of directional properties of the *d*-band bonding introduced by the AF ordering. Magnetically induced tetragonal distortions have also been discussed within a tight-binding framework by Krüger *et al.*[61]

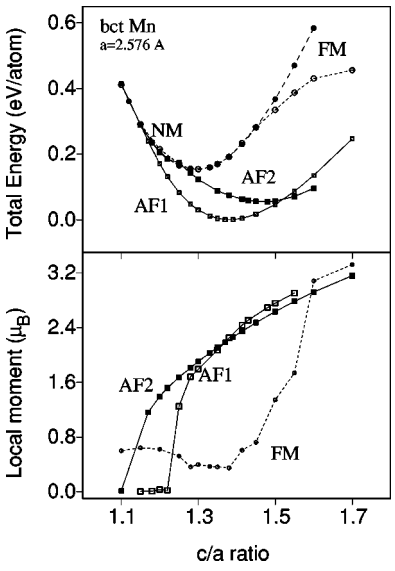

FIG. 3. Total energy and magnetic moment as a function of volume for the NM (full circles), FM (open cirles), AF1 (open box), and AF2 (full box) phases of bct Mn calculated in the GGA. The energy is given relative to the AF1 ground state.

The epitaxial constraint leads also to a further stabilization of the AF1 over the AF2 and FM phases. For the AF2 bct Mn phase, the c/a ratio is expanded beyond the ideal value, i.e., the interlayer distance perpendicular to the interface with the substrate is expanded. This is a consequence of the larger equilibrium volume of the AF2 phase. The magnetic energy difference is also slightly increased. The FM state in bct Mn with fixed in-plane distance $a_0=2.576$ Å is unstable, the magnetic moment is strongly reduced and the lowest energy for the FM and the energetically almost degenerate NM phase is found at $c/a=1.30$, i.e., for strongly reduced interplanar distances.

C. Free-standing Mn monolayers: Structural and magnetic properties

The differences in the prediction of the magnetic ground state due to the gradient corrections are also very pronounced for free-standing Mn monolayers. For the square lattice, the calculation has been performed for a $c(2\times2)$ cell accommodating both the NM and AF states. For the hexagonal lattice, a $(2\times\sqrt{3})$ cell has been used, in the AF state the moments located at the corners and at the center of this cell show opposite orientations. One should point out that with the triangular nearest-neighbor geometry of the hexagonal lattice, this type of AFM ordering is necessarily partly frustrated and the true ground state is possibly more complex, eventually noncollinear. Figure 4 compares the total energies for the AF and NM phases of the square [(100) plane] and close-packed hexagonal [(111) plane] Mn monolayers as a function of the interatomic distance calculated using both the LSDA and GGA. The two calculations make different predictions for the ground state. The AF square lattice has the lowest energy in the LSDA, while the GGA stabilizes the hexagonal AF

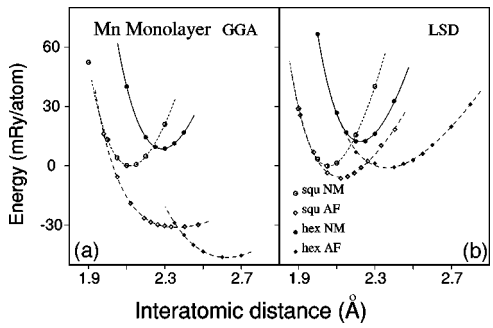

FIG. 4. Total energy as a function of interatomic distances of nonmagnetic (NM), and antiferromagnetic (AF) square (SQU) and hexagonal (HEX) unsupported Mn monolayer. (a) GGA and (b) LSD USPP calculations.

layer. In the GGA, antiferromagnetism also reverses the stability of the square and hexagonal lattices compared to the paramagnetic case, whereas the same sequence is retained in the LSDA. Our calculations have also considered the possibility of a ferromagnetic state: for both structures, a FM phase is energetically more favorable than the NM phase, but distinctly less than the AF phase (see Table II). Due to the reduced coordination, a high-moment state is favored for both FM and AF phases: for the FM monolayers, the magnetic moment at equilibrium is with 4.3 to 4.5μ_B close to the limit set by Hund's rule, the AF moments are lower, but distinctly higher than in the bulk (3.0μ_B for the square, 3.6 μ_B for the hexagonal layer). Magnetism also has a strong influence on the equilibrium distances: in the FM phase the nearest-neighbor distance is expanded by about 20% compared to the NM case, in the AF state the expansion is somewhat lower. This is as expected from the size of the magnetic moments. Compared to bulk AF fcc Mn, however, the interatomic distance in the AF square lattice is reduced by nearly 9%, as a consequence of the increased bond strength due to the reduced coordination. For the FM square layer, the equilibrium distance is slightly larger than in the metastable high-spin FM fcc phase. Altogether these results suggest that magnetic effects related to gradient corrections are even more pronounced in thin layers than in the volume.

IV. HOMOGENEOUS MN OVERLAYERS ON CU(100)

We first discuss the results of *ab initio* calculations for structurally relaxed homogeneous Mn overlayers on Cu(100). In our slab (= film+substrate) model we allow the relaxation of the atoms in the Mn overlayer and in three to five monolayers of the Cu substrate.

TABLE II. Total-energy difference ΔE_s relative to the stable hexagonal AF lattice, nearest-neighbor distance a_0, and magnetic moment $|m_0|$ at equilibrium for the NM, FM, and AF phases of square and hexagonal Mn monolayers, calculated in the GGA.

	Lattice	Phase	E_c (eV/cell)	a_0 (Å)	$\|m_0\|$ (μ_B)
	square	NM	0.629	2.117	0.0
GGA	square	FM	0.454	2.656	4.46
	square	AF	0.208	2.355	3.03
	hexag.	NM	0.748	2.286	0.0
GGA	hexag.	FM	0.260	2.747	4.32
	hexag.	AF	0.000	2.622	3.61

TABLE III. Magnetic and structural properties of a 1-ML Mn/Cu(001) film. E_c is the total energy per unit cell, m_i are the magnetic moments in the ith layer, Δd_{ij} the changes in interlayer distances, $\Delta z^{\uparrow(\downarrow)}$ give the relaxation of an atom in the direction perpendicular to the surface. The unit cell is a $c(2\times2)$ slab with altogether 11 layers.

Phase	E_c (eV)	Layers	m_i (μ_B)	Δd_{ij} (%)	$\Delta z^{\uparrow}$ ($\Delta z^{\downarrow}$) (%)
AF	−78.89	1st L Mn	±3.75		4.60 4.80
		2nd L Cu	0.02		−1.42 −1.42
		3rd L Cu	0.01		−1.93 −1.93
		4th L Cu	0.01		−1.03 −1.03
FM	−77.52	1st L Mn	3.86	6.38	
		2nd L Cu	0.03	0.60	
		3rd L Cu	−0.01	0.11	
		4th L Cu	0.00	0.39	
NM	−76.60	1st L Mn		−1.74	
		2nd L Cu		1.15	
		3rd L Cu		−0.23	
		4th L Cu		0.09	

A. 1-ML Mn/Cu(001)

1. Magnetism and magnetostructural effects

We have calculated the structural and magnetic properties of 1-ML Mn/Cu(001) in the $p(1\times1)$ FM, NM, and $c(2\times2)$ AF configurations. We demonstrate that the magnetic state of the adlayer profoundly influences its structure. The substrate has been modeled by a ten-layer slab with the lattice parameter of fcc Cu ($a_0=3.643$ Å). Table III lists the total cohesive energies, local magnetic moments, and atomic relaxations perpendicular to the surface for all three magnetic states of the overlayer. The relaxation is measured in terms of the change of the interlayer distances d_{ij} for the FM and NM phases, the local atomic relaxations Δz of the inequivalent Mn and Cu atoms in the $c(2\times2)$ cell are given for the AF phase (in percent of the interlayer Cu-Cu equilibrium distance of $a_0/2$). The AF Mn overlayer is the most stable and the total-energy differences of the FM and NM configurations are very large, 1.37 and 2.29 eV/unit cell [the $c(2\times2)$ slab with 22 atoms]. Both the AF and the FM phases of the overlayer are in a high-spin state, with magnetic moments that are for the AF configuration ($m_0=\pm3.75\mu_B$) even larger than for the free-standing square monolayer. This enhancement is due to increased Mn-Mn distance. For the FM phase, the epitaxial strain resulting in a closer Mn-Mn distance than in the free monolayer also results in a reduction of the magnetic moment.

Magnetovolume effects due to the strongly enhanced magnetic moments also lead to structural relaxations in spite of the excellent lattice match between fcc AF Mn and the Cu substrate. In the $c(2\times2)$ AF phase, Mn atoms relax outward

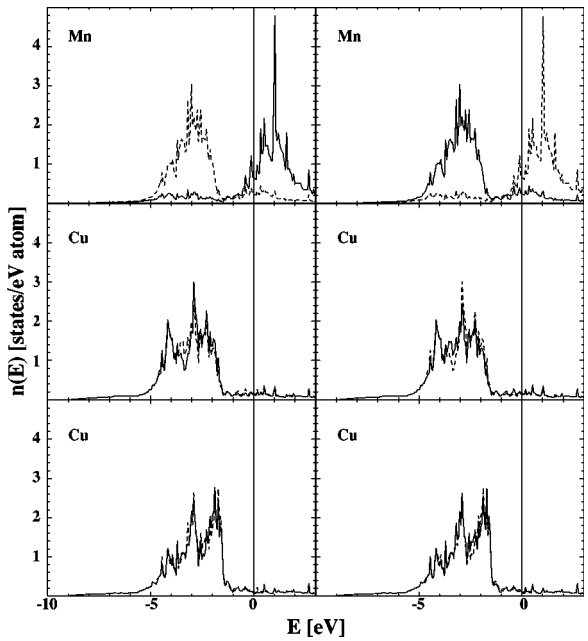

FIG. 5. Layer resolved spin-polarized density of states for the top three layers of the 11-layer slab representing AF $c(2\times2)$ 1-ML Mn/Cu(001). The spin-up components are represented by solid lines and the spin-down components by dashed lines. Left and right panels represent the two inequivalent sites in the $c(2\times2)$ surface cell. The energy is given relative to the Fermi level.

by about 0.1 Å, but display only a negligible buckling of less than 0.01 Å. In the Cu substrate, a slight contraction of the interlayer distances is predicted. Close to the interface, this contraction is smaller than at the free Cu(100) surface [$\Delta d_{12} = -3.04\%$ (GGA), -2.4% (experiment, see Ref. 62)], but it extends to deeper layers while for the pure Cu surface the relaxation of the subsurface layers is nearly three times smaller. For an FM Mn overlayer, the outward relaxation is more pronounced, but the substrate is less affected. A nonmagnetic overlayer would even show a weak inward relaxation.

2. Electronic structure and exchange splitting

Figure 5 shows the layer-resolved spin-polarized electronic density of states (DOS) of AF $c(2\times2)$ Mn/Cu, Fig. 6 the electronic dispersion relations calculated for the 11-layer slab. In the Mn-DOS we find a large spin splitting (measured in terms of the positions of the maxima in the *d*-band DOS for spin-up and spin-down states) of about 4 eV. Compared to bulk AF1 fcc Mn, the width of the majority-spin band is strongly reduced from about 5 to 3 eV, a similar narrowing is also observed for the minority-spin DOS which shows only a weak overlap with the Fermi level. The *d* band of the Cu layer at the interface shows only a very slight narrowing, more important is the modification of the form of the band resulting from the Cu-Mn hybridization. The analysis of the dispersion relations of the eigenstates shows that surface states exist only above the Fermi level. The localization of surface states is characterized in Fig. 6 by three different degrees of shading of the dots marking the dispersion of surface states, indicating 90, 75, and 60% localization of the state in the Mn overlayer. Surface states are detected only in

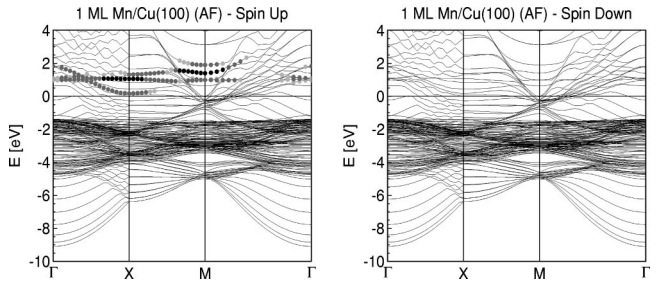

FIG. 6. Electronic dispersion relations of an 11-layer slab representing AF $c(2\times2)$ 1-ML Mn/Cu(001). Surface states are defined as states concentrated to 60 (75, 90)% on one Mn atom in the surface layer and represented by light grey (dark gray, black) dots in the figures marking the dispersion relations. The energy is given relative to the Fermi level.

the unoccupied majority-spin states. We find an almost dispersionless surface band at ~ 1 eV and at about 1.5 eV centered around the *M* point, as well as a band of less strongly localized states along Γ-*X* with a strong downward dispersion almost reaching the Fermi level near *X*.

B. 2-ML Mn/Cu(001)

1. Magnetism and magnetostructural effects

The AF, FM, and NM configurations of the 2-ML Mn/Cu(001) have been calculated for a $p(1\times1)$ slab with 9 Cu substrate layers and 2 Mn overlayers. Here, we consider a layered antiferromagnetism corresponding to the bulk AF1 type. In-plane $c(2\times2)$ antiferromagnetism is unstable for two or more Mn layers. As shown in Table IV the AF configuration is more stable than the FM and NM configurations by 0.26 and 1.10 eV/unit cell, respectively. These structural energies refer to a unit cell with 22 atoms, to allow a comparison with the 1-ML case. The change in the AF structure does not lead to a large change in the magnetic moments at the free surface: for the 2-ML overlayer we find a Mn moment of $3.45\mu_B$ (compared to $3.75\mu_B$ in the monolayer

TABLE IV. Magnetic and structural properties of a 2-ML Mn/Cu(001) film. The unit cell is a $c(2\times2)$ slab with altogether 11 atomic layers. For the notation, see Table III.

Phase	E_c (eV)	Layers	m_i (μ_B)	Δd_{ij} (%)
AF	−77.38	1st L Mn	3.45	3.37
		2nd L Mn	−3.06	5.00
		3rd L Cu	−0.05	0.47
		4th L Cu	0.00	−0.42
FM	−77.12	1st L Mn	3.57	3.63
		2nd L Mn	3.02	5.88
		3rd L Cu	0.04	0.46
		4th L Cu	0.00	−0.57
NM	−76.28	1st L Mn		−30.86
		2nd L Mn		5.99
		3rd L Cu		−0.84
		4th L Cu		−0.15

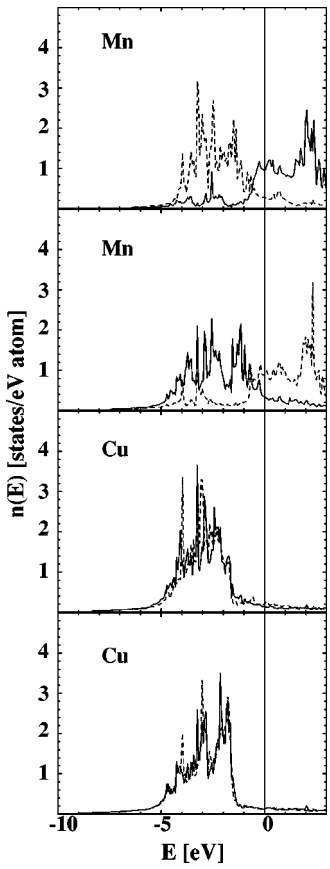

FIG. 7. Layer resolved spin-polarized density of states for the top four layers of an 11-layer slab representing AF $p(1\times1)$ 2-ML Mn/Cu(001). The spin-up components are represented by solid lines and the spin-down components by dashed lines. The energy is given relative to the Fermi level.

limit). For the subsurface Mn layer the local moment is reduced to $-3.06\mu_B$. This means that the antiferromagnetism is not completely compensated and that the complete Mn bilayer has a net magnetic moment of about $0.19\mu_B$/Mn atom. The moments calculated for the FM overlayer are of similar magnitude. For both the AF and FM states, we notice that the second Mn layer relaxes outward by about 5% which is comparable with the outward relaxation of Mn in 1-ML Mn/Cu(001), while for the surface Mn atoms the relaxation is smaller since the expansion caused by the epitaxial constraint is superposed by an inward relaxation due to surface effects. The rather modest outward relaxation of Mn atoms in the AF and FM cases must be confronted to a dramatic inward relaxation by 0.55 Å ($d_{ij}=-30.9\%$) predicted for NM 2-ML Mn/Cu(001). This illustrates the importance of the magnetism in the Mn layer for the structure of Mn films on Cu.

2. Electronic structure and exchange splitting

Figure 7 shows the spin-resolved electronic density of states and Fig. 8 the dispersion relations of electronic surface states in the 2-ML Mn/Cu(100) system for the stable layered antiferromagnetic configuration. Compared to the 1-ML system we find a less pronounced shift of the *d* band of the Mn-majority states in both the surface and the subsurface layers to higher binding energies—for the subsurface layer,

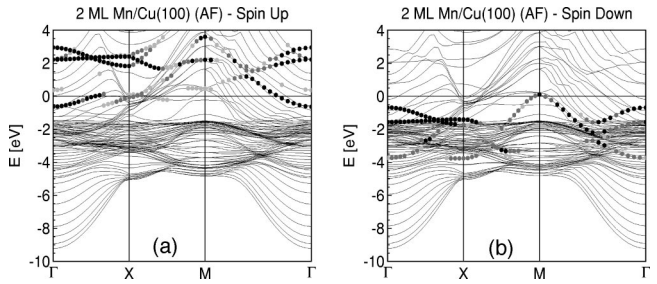

FIG. 8. Electronic dispersion relations for AF $p(1\times1)$ 2-ML Mn/Cu(001). Surface states are defined as states concentrated to 60 (75, 90)% on the Mn atom in the first Mn layer (a), and on the Mn atom in the second layer (b) and represented by light grey (dark gray, black) dots in the figures marking the dispersion relations. The energy is given relative to the Fermi level.

the *d* band shows even a weak overlap with the Fermi level. As a consequence, the overlap of the Mn and Cu *d* bands is reduced. Whereas for the Mn monolayer, we had found predominantly dispersionless surface states only above the Fermi level, very intense occupied surface states with considerable dispersion are found both in surface and in the subsurface layers close to the upper edge of the Mn *d* band. Comparing the surface states for spin-up and spin-down electrons, we find that the surface bands are to a first approximation shifted rigidly according to a Stoner picture. For the surface state at the *M* point we find an exchange splitting of ~3.6 eV, for the states at the Γ point, the splitting is about 3.7 eV. For the states localized in the subsurface Mn layer, the exchange splitting at the same symmetry points is reduced to about 3.1 and 3.4 eV, in correspondence to the smaller magnetic moments. From the ratio of exchange splitting to magnetic moments we can estimate a Stoner parameter $I=\Delta E_{exch.}/m_0$ of about 1 eV/μ_B, which is the same as in bulk transition metals.

V. SURFACE ALLOYS

A. 1-ML CuMn/Cu(001)

1. Magnetism and magnetostructural effects

Ordered FM and NM CuMn alloys on Cu(001) have been modeled in the monolayer limit using a $c(2\times2)$ slab with ten Cu substrate layers. In the relaxed structure the FM configuration is more stable than the NM configuration by about 2.26 eV/cell. No AF solution could be found, a spin-polarized calculation always converged to the FM state. The corresponding magnetic and structural properties of 1-ML CuMn/Cu(001) are summarized in Table V. A buckling of about 0.3 Å is predicted for the surface layer, the Mn atoms carrying a large magnetic moment of $4.09\mu_B$ moving outward by 9.3% of the unrelaxed interlayer distances, while the Cu atoms with a small induced moment of only $0.05\mu_B$ move inwards by 5%. The Mn atoms in the surface alloy have a local moment that is nearly $0.4\mu_B$ larger than the moments in the FM (or AF) pure Mn monolayer. This is related to the larger Mn-Mn bond distance and a stronger hybridization (bonding) of Cu and Mn majority spin states. The Cu atoms in the first substrate layer show only a small buckling and no global relaxation. In the hypothetical NM surface alloy Mn and Cu atoms at the surface relax inward,

TABLE V. Magnetic and structural properties of a 1-ML CuMn/Cu(001). The unit cell is a $c(2\times2)$ slab with 11 atomic layers. For the alloy layers values in parentheses refer to the Mn atoms. The Δz_{ij} give the relaxation of the inequivalent atoms in each layer along the direction perpendicular to the slab. For the remaining notations, see Table III.

Phase	E_c (eV)	Layers	m_i (μ_B)	Δz_{ij} (%)
FM	−79.66	1st L Cu(Mn)	0.05 (4.09)	−4.98 (9.34)
		2nd L Cu	0.01 −0.01	0.71 −0.71
		3rd L Cu	0.01 −0.01	−0.30 −0.30
		4th L Cu	0.01 −0.00	−0.32 −0.32
NM	−77.40	1st L Cu(Mn)		−0.84 (−2.65)
		2nd L Cu		1.46 1.46
		3rd L Cu		0.58 0.55
		4th L Cu		0.41 0.41

while the Cu atoms in the substrate layer relax outward (the relaxation being slightly stronger than for the ferromagnetic configuration).

2. Electronic structure and exchange splitting

Figure 9 shows the spin-polarized electronic density of states of the 1-ML CuMn/Cu(100) alloy, Fig. 10 displays the dispersion relations of the surface states. For the nonmagnetic configuration (not shown here) the Mn DOS has the character of a very narrow impurity band (with a width at half maximum hardly exceeding 1 eV) centered at the Fermi level and only a weak overlap with the Cu DOS in the alloy

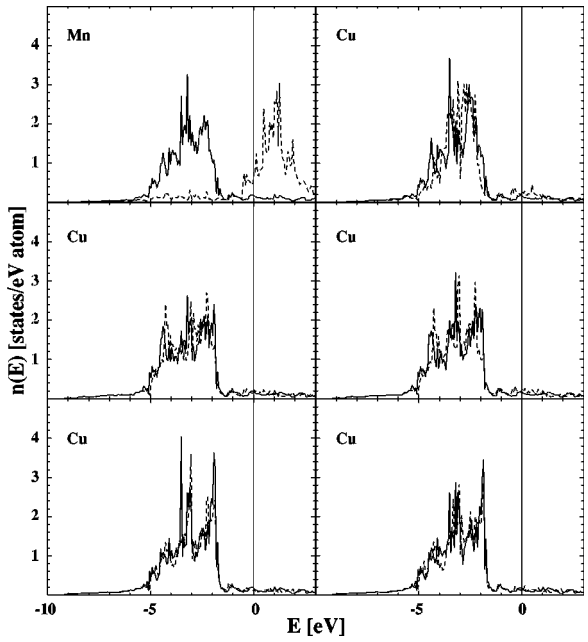

FIG. 9. Layer resolved spin-polarized density of states for the top three layers in FM $c(2\times2)$ 1-ML CuMn/Cu(001). The spin-up components are represented by solid lines and the spin-down components by dashed lines. Left and right panels represent the DOS on the two inequivalent sites in the $c(2\times2)$ cell. The energy is given relative to the Fermi level.

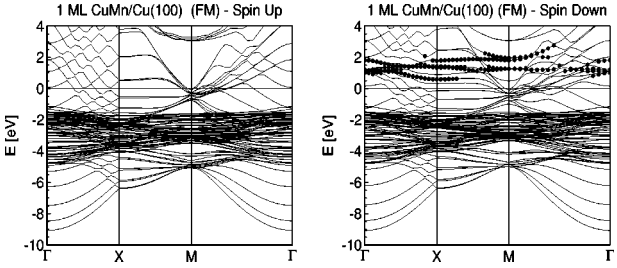

FIG. 10. Electronic dispersion relations for FM $c(2\times2)$ 1-ML CuMn/Cu(001). Surface states are defined as states concentrated to 60 (75, 90)% on one Mn atom in the surface layer which are represented by light grey (dark gray, black) dots in the figures marking the dispersion relations. The energy is given relative to the Fermi level.

layer. The DOS of the FM surface alloy, on the other hand, is quite similar to that of the AF Mn monolayer on Cu(100): There is a large overlap between the Cu *d* band of the alloy layer and of the substrate and the *d* band of the Mn-majority states, with the upper edge of the band located about 1.9 eV below the Fermi level. The Mn-minority band is shifted almost entirely above the Fermi level and because the Cu-Mn hybridization is much weaker, the bandwidth is lower than for the majority band. The *d* band of the Cu atoms in the alloy layer is weakly spin polarized, with a distinctly lower width for the minority band because of a weaker hybridization with the Mn states. The dispersion relations of the surface states plotted in Fig. 10 show that only in the Mn-minority band surface states with appreciable intensity are found, no surface states localized on the Cu atoms of the surface alloy could be identified.

From the positions of the most intense empty surface state at the *X* point at about 1.4 eV and the weak occupied surface state at −3.1 eV we estimate an exchange splitting of about 4.5 eV. This estimate agrees rather well with the distance between the main peaks in the majority and minority Mn *d* bands ($E_\uparrow=-3.2$ eV, $E_\downarrow=1.2$ eV, $\Delta E=4.4$ eV). Together with the magnetic moment of $4.1\mu_B$ this points to an effective Stoner-I that is slightly larger than, but still comparable with the values calculated for the bulk Mn phases and for homogeneous Mn overlayers on Cu.

Our DOS for the monolayer surface alloy is quite different from the LSDA results reported by Rader *et al.*[29] Their results for $c(2\times2)$ FM MnCu show an impurity-like narrow Mn *d* band for both majority and minority states located at −1.55 and +1.13 eV and hence a significantly smaller exchange splitting of only 2.7 eV, although their calculated magnetic moment is with $3.75\mu_B$ only slightly lower than our value. The result of Rader *et al.* for the Cu-Mn surface alloy is the more surprising because for the isostructural $c(2\times2)$ FM MnNi /Ni(100) surface alloy they report the formation of a very broad Mn *d* majority band together with a narrow minority band, in accordance with recent LMTO calculations of Spišák and Hafner[63] for MnNi alloy layers and with the present results for CuMn alloy layers. From the positions of the *d* bands of the pure metals, one would rather expect the hybridization to be weaker for Ni-Mn than for Cu-Mn. We shall return to this point when we discuss the comparison of the calculated spectra with the available experimental data.

TABLE VI. Magnetic and structural properties of a 2-ML CuMn/Cu(001). The unit cell is a $c(2\times2)$ slab with 11 atomic layers. For the notation, see Tables III and V.

Phase	E_c (eV)	Layers	m_i (μ_B)	Δz_{ij} (%)
AF	−79.14	1st L Cu(Mn)	0.06 (4.13)	5.66(18.42)
		2nd L Cu(Mn)	−0.03 (−3.66)	1.65 (6.23)
		3rd L Cu	−0.02 −0.03	1.09 0.60
		4th L Cu	0.00 0.01	0.48 −0.08
NM	−77.41	1st L Cu(Mn)		4.65 (−17.86)
		2nd L Cu(Mn)		−4.65 (13.98)
		3rd L Cu		1.89 0.22
		4th L Cu		0.90 0.48

B. 2-ML CuMn/Cu(001) surface alloys

1. Stability, magnetism, and structure

The stability of the surface alloy beyond the monolayer limit and with respect to a homogeneous Mn overlayer has been addressed by computing the 2-ML CuMn/Cu(001) case. In this case we have an equal number of Cu and Mn atoms in the unit cell than for 1-ML Mn/Cu(001) so that the computed energies are directly comparable. We have considered a NM and a layered AF configuration consisting of $c(2\times2)$ FM CuMn layers with antiparallel orientation. The results compiled in Table VI show that the AF surface alloy is energetically more favorable by -1.73 eV/unit cell. In the AF configuration the Mn atoms in the surface layer carry a large magnetic moment of $4.13\mu_B$ and relax outward by 18.4%. The Cu atoms in the surface layer show only a very small induced magnetic polarization and relax outward by 5.6%. Hence the buckling of the surface layer is with 12.8% only slightly weaker than for the alloy monolayer where we had found a buckling of 14.3%. Mn atoms in the subsurface layer show a smaller magnetic moment ($-3.66\mu_B$) and only a smaller outward relaxation. Cu atoms in the subsurface layer show only a very modest outward relaxation, resulting in a buckling of 4.6%. Magnetism has a pronounced influence on the structure of the surface alloy: in the nonmagnetic configuration the Mn atoms in the surface layer show a large inward relaxation, whereas the Mn atoms in the subsurface layers relax outward by about the same amount. Cu atoms in both layers relax in the direction opposite to the Mn atoms. This leads to a corrugation of both alloy layers (by 0.41 and 0.34 Å) which is substantially larger than the corrugation calculated for the AF surface alloy ($\Delta z=0.23$ and 0.08 Å in the surface and subsurface layers, respectively).

The cohesive energies compiled in Table VI confirm the stability of the AF surface alloy with a formation energy of $\Delta H=-0.25$ eV/cell compared with the homogeneous AF Mn/Cu(001) overlayer. In the NM configurations, the heat of formation of the surface alloy would even be higher, $\Delta H=-0.81$ eV/cell. This is due to the fact that the magnetic energy difference between the AF and NM phases is larger for the homogeneous Mn overlayer than for the surface alloy. Hence the stability of the the surface alloy is not magnetically induced, but arises from the formation of strong covalent Cu-Mn bonds.

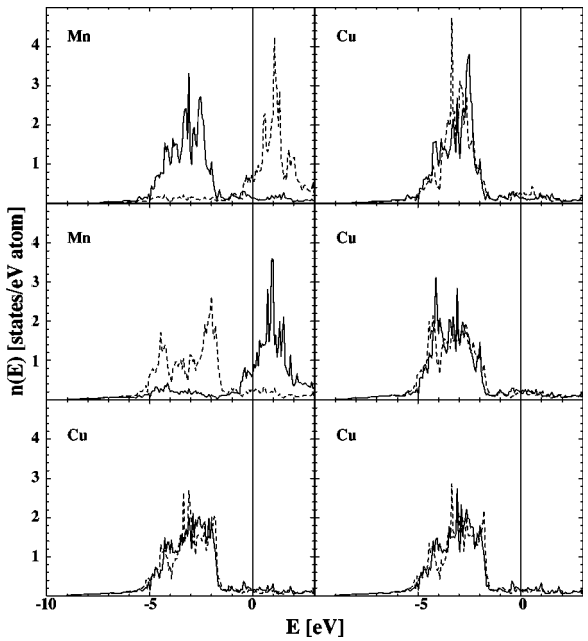

FIG. 11. Layer resolved spin-polarized density of states for the top three layers in AF $c(2\times2)$ 2-ML CuMn/Cu(001). The spin-up components are represented by solid lines and the spin-down components by dashed lines. Left and right panels refer to the two inequivalent sites in the $c(2\times2)$ cell. The energy is given relative to the Fermi level.

2. Electronic structure and exchange splitting

Figure 11 shows the spin-polarized electronic density of states calculated for the 2-ML CuMn surface alloy. We find a substantial difference in the Mn *d* majority bands: while the Mn *d* band of the surface atoms has unimodal character, with a main peak at about -3 eV, the *d* band of the Mn atoms in the subsurface layer shows a strong bonding-antibonding splitting with the main (antibonding) peak at -2 eV. The minority bands on the other hand are quite similar, with the principal peak at about 1 eV. This means that the reduced magnetic moment in the subsurface layer is also reflected in a smaller local exchange splitting. The analysis of the dispersion relations shows that surface states with appreciable intensity are found only in the minority bands of the Mn atoms in both the surface and subsurface layers. The exchange splitting estimated from the positions of the most intense surface states agrees well with the values derived from the main peaks in the spin-polarized DOS ($\Delta E\sim4$ eV in the surface layer, $\Delta E\geqslant3$ eV in the subsurface layer), it is slightly smaller than for the alloy monolayer.

VI. DISCUSSION AND COMPARISON WITH EXPERIMENT

A. Stability and structure of CuMn surface alloys

In agreement with experiment[25] we find that the formation of a $c(2\times2)$ surface alloy is energetically more favorable than the formation of a homogeneous Mn overlayer. Experimentally it is found that films deposited at temperatures higher than 270 K form a stable $c(2\times2)$ alloy phase up to a thickness of 2.25 ML's. LEED analyses[30] show a strong

buckling of $\Delta z = 0.30 \pm 0.02$ Å in the surface layer at a total Mn-coverage of 0.5 ML's and only a very weak buckling in the subsurface layer. This agrees very well with our prediction of a buckling of $\Delta z = 0.26$ Å for the AF alloy layer. A somewhat larger outward relaxation of the Mn atoms relative to the surrounding alloy-layer Cu atoms of 0.39 ± 0.08 Å has been reported by Toomes *et al.* on the basis of photoelectron diffractions studies,[64] but this is still consistent with the previous LEED studies within the quoted accuracies.

B. Magnetism of CuMn surface alloys

For the stable CuMn alloy layers, magnetic moments of about $4.1\mu_B$ are predicted for the Mn atoms in the surface layer, decreasing slightly in the subsurface layer. These large moments are distinctly higher than those computed for homogeneous Mn overlayers. The high-spin state of Mn is in agreement with the soft x-ray adsorption and x-ray magnetic circular dichroism studies of O'Brien and Tonner[26] and the combined photoemission and inverse photoemission studies,[27–29] although no quantitative assessment of the magnitude of the magnetic moments can be deduced from the experiment (concerning the observed exchange splitting, cf. the following subsection). The high-spin state of Mn is responsible for the large observed buckling, arising from the outward relaxation of the Mn atoms induced by the large magnetovolume effect characteristic for Mn: for a nonmagnetic CuMn alloy layer, the calculations predict in the monolayer limit only a very weak buckling (with the Mn atoms moving slightly inward). For the NM 2-ML CuMn case a large buckling is predicted, but with the surface Mn atoms moving inward instead of outward. Also for the homogeneous Mn overlayers magnetism turns an inward relaxation (which is very large for the 2-ML case) into an outward relaxation.

Magnetism is, however, not responsible for the surface alloying: at a total coverage of one ML intermixing leads to an even larger energy gain in the nonmagnetic case than when we compare the respective magnetic ground states. The reason is that the magnetic energy difference is larger for the $c(2\times2)$ in-plane AF of the overlayer than for the layered AF of the surface alloy.

C. Comparison with previous LSDA studies

Previous density-functional studies of surface alloying and magnetism in the CuMn/Cu(001) system have been reported by Wuttig *et al.*[30] in the local-density approximation and by Asada and Blügel[65] using generalized gradient corrections. Compared to our results for 1-ML CuMn/Cu(001) the LSDA calculations performed using the full-potential augmented plane-wave (FLAPW) method predict a slightly larger outward relaxation of the MN atoms by $\Delta z_{Mn} = 11.5\%$ and a slightly smaller inward relaxation of the Cu atoms of $\Delta z_{Cu} = -2.5\%$, i.e., an almost identical buckling of 14% at a smaller Mn moment of only $3.64\mu_B$. The difference in the magnetic moments has to be largely attributed to the difference between the LSDA and the GGA resulting in a larger lattice constant for the Cu substrate, as well as to the suppression of the substrate relaxation in the FLAPW. The almost equal buckling is result of a compensation between the larger magnetic moment in the GGA resulting in a larger magnetovolume effect and the larger Cu-lattice constant reducing the local strain around the Mn sites. Asada and Blügel[65] have extended the FLAPW studies to account for generalized gradient corrections, but performed calculations only for the ideal fcc geometry.

D. Electronic structure and photoelectron spectroscopy

The calculated electronic structure can be compared with the available data from photoemission and inverse photoemission spectroscopies (PES and IPES). For a comparison of our results with the measured angle-integrated photoemission intensities we compute an average of the local angular-momentum-decomposed densities of states, weighted with the partial photoionization cross sections (we take the values tabulated by Yeh and Lindau[66]), multiply with a Fermi function, and fold with a Gaussian to account for the limited experimental resolution. Because of the rather low photon energies used in the experiments, an escape depth of the photoelectrons of three monolayers has been assumed. For the inverse photoemission intensities we proceed accordingly. Figure 12 confronts the calculated results with the experiments of Rader *et al.*[29] (angle-resolved and integrated ultraviolet PES with photon energies of $\hbar\omega = 40$ and 58 eV, IPES at incident electron energies of $E_i = 14.5$ eV), Binns and Norris[28] (PES at a photon energy of 21.2 eV), and Hayden *et al.*[27] (angle-resolved IPES at incident electron energies of 10 and 11.5 eV). Part (a) shows the results obtained for the pure Cu(001) surface and confirms the validity of our assumptions concerning the calculation of the PES and IPES intensities.

1. Probing the exchange splitting in the monolayer limit

In part (b) of Fig. 12 we confront our results for the FM CuMn-alloy monolayer with the PES and IPES intensities of Rader *et al.* and with the IPES spectra of Hayden *et al.* for the same nominal coverage. The analysis of the PES data is complicated by the fact that the photoionization cross section of Mn shows a resonance at photon energies above 50 eV, so that the tabulated data are probably not so good a reference—in the calculated spectra the Mn contribution is certainly quite severely underestimated. The main contribution from the Mn majority-spin states is represented by the peak at -3.24 eV (theory) and -3.7 ± 0.3 eV (experiment). In the IPES data of Rader *et al.* the weak peak just above the Fermi level represents the empty Cu-s,p band, the peak at 1.85 eV the Mn minority spin states while the peak at about 3.7 eV is an image potential state. In our calculation, the Mn minority-spin peak is located at about 1.2 eV. Together this means that the LSDA+GGC calculations underestimate the exchange splitting. $\Delta E = 4.4$ eV (theory) compared to $\Delta E = 5.5 \pm 0.3$ eV (experiment). The IPES data of Hayden *et al.* recorded at a somewhat lower energy of the incident electrons are characterized by a much larger contribution from the Cu substrate which makes the identification of the Mn contributions much more difficult. The small peak at about 2 eV assigned to the Mn-minority states agrees quite well with the analysis of Rader *et al.* The angular resolved spectroscopies yield also some information on the dispersion of surface states. Hayden *et al.* identify an empty Mn-surface state at about 2 eV with almost no dispersion—in good

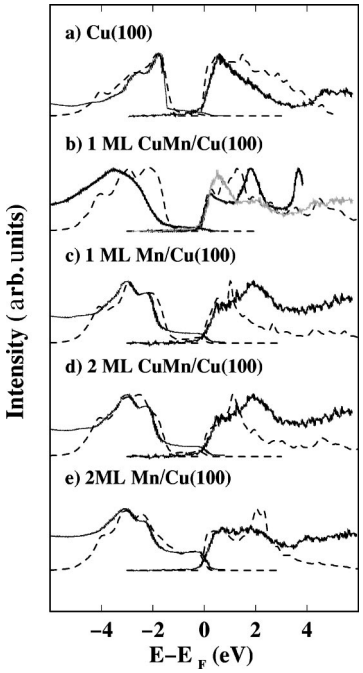

FIG. 12. Comparison of computed (dashed lines) and experimental UPS and IPES spectra (solid lines). The calculated spectra for (a) clean Cu(100) are compared with Refs. 27 and 28, (b) 1-ML CuMn/Cu(100) with Refs. 29 and 28 (grey), (c) 1-ML Mn/Cu(100) with Refs. 27 and 28, (d) 2-ML CuMn/Cu(100) with Refs. 27 and 28, and (e) 2-ML Mn/Cu(100) with Refs. 27 and 28 [thick Mn film on Cu(100)]. The energy is given relative to the Fermi level.

agreement with the analysis of Rader *et al.* and with our results shown in Fig. 10. Since the Mn-majority band largely overlaps with the Cu *d* band, no identification of Mn-induced surface states is possible. The most important difference between theory and experiment is the discrepancy in the exchange splitting. We believe that this difference arises mostly from final-state effects in both PES and IPES tending to shift the peaks in the occupied and empty parts apart: our calculations provide eigenvalues for the neutral ground state, whereas the experiments are performed for the positively (PES) or negatively (IPES) charged final state. The additional Coulomb interaction lowers the hole state and raises the energy of the electron state. The FLAPW calculations of Rader *et al.* [29] produce an even lower exchange splitting of only 2.7 eV, the difference arising mainly from the position of the Mn-majority states forming a very narrow, almost impuritylike band around -1.55 eV. The result is strange, because the calculated exchange splitting is even substantially smaller than that calculated by Rader *et al.* for 1-ML NiMn/Ni(001), in contrast to the trend found in the experiment. The difference cannot be attributed to an LSD/GGA effect and remains puzzling for the moment.

The value of the exchange splitting is also a valuable information on the magnitude of the magnetic moments. Himpsel *et al.*[67] have pointed out on the basis of PES and IPES experiments that for a wide variety of ferromagnetic and antiferromagnetic systems, ranging from the free atoms to bulk metals and alloys, the ratio $I=\Delta E/m$ between the exchange splitting and the magnetic moment corresponds to a universal value of the Stoner parameter I of $I=1$ eVμ_B^{-1}. Turek *et al.*[68] have demonstrated that LSD calculations lead to the same conclusion and that this correlation holds even on a local level, i.e., in inhomogeneous materials the local fluctuations in the exchange splitting follow the same trend as the fluctuations in the magnetic moments. The results presented here conform with these conclusions: for all systems we find $I\sim 1\pm 0.1$ eVμ_B^{-1}. Hence the observed exchange splitting may be considered as a direct evidence for the high-moment state of Mn.

2. Homogeneous Mn overlayers

In Fig. 12(c) and 12(d) we compare the PES results of Binns and Norris[28] and the IPES data of Hayden *et al.*[27] for a coverage of 1-ML Mn with our results for a homogeneous AF Mn-overlayer (cf. the DOS shown in Fig. 5) and for the 2-ML CuMn-layer (cf. the DOS given in Fig. 11. We note at once that at the level of resolution of the PES and IPES experiments, alloying does not result in very striking differences. Only the occupied valence band has somewhat more structure and the empty bands are slightly narrower for the homogeneous Mn overlayer. While the agreement for the occupied bands is quite satisfactory (the experiments have been performed at low photon energies outside the resonant regime, so that the photoionization cross section now leads to a more realistic weighting of the Cu and Mn contributions), the same discrepancy already found for the alloy monolayer appears in the IPES spectra: the final-state effects shift the peak induced by the Mn-minority states to energies at about 2 eV. Let us note that the extent of the final-state effect depends on the degree of localization of the Mn states, it is natural that this effect is more pronounced for the minority states.

3. Thicker Mn layers

Finally we compare in Fig. 12(e) our results for the Mn bilayer with the experimental results on thicker Mn films where alloying is suppressed because of the limited interdiffusion rate (cf. Fig. 7 for the corresponding DOS). We find that the increasing thickness has only a rather weak effect on the occupied band, except for the increasing intensity just below the Fermi level resulting from the broadening of the Mn-majority band. The broadening is even stronger for the Mn-minority band: instead of a unimodal DOS like in the Mn monolayer, the bonding-antibonding splitting leads to a two-peaked Mn DOS with the bonding minority states overlapping with the Fermi level. This also results in a reduction of final-state effects so that we now observe a good agreement with both PES and IPES experiments.

VII. CONCLUSIONS

In this paper we have presented a detailed analysis of the structural and magnetic properties of Mn in its bulk phases, in free-standing monolayers, and in thin films epitaxially grown on Cu(100) substrates. The first important conclusion is that nonlocal corrections to the local-density exchange-correlation effects in the form of generalized gradient corrections are decisive for a correct description of the magneto-structural properties of Mn. This result confirms and extends earlier studies of the bulk crystalline phases. We also show that the effect of the GGC's is even more pronounced in two than in three dimensions, as illustrated for the Mn monolay-

ers. The second important conclusion is that in thin layers Mn assumes a high-moment state with $m \sim 4\mu_B$, i.e., not too far below the limit of $5\mu_B$ set by Hund's rule. From the comparison of exchange splitting (we find values of $\Delta E \geqslant 4$ eV) and magnetic moments we can conclude that even in its high-moment state Mn is well characterized as an itinerant magnet with a Stoner parameter of $I \sim 1$ eVμ_B^{-1}. The strong hybridization between the Mn and Cu *d* bands leads to a strong covalent Cu-Mn interaction so that the formation of a surface alloy is energetically more favorable than the formation of a homogeneous overlayer. Because second-neighbor Mn-Mn interactions are ferromagnetic, an ordered $c(2\times2)$ CuMn surface alloy is ferromagnetic in the monolayer limit. The ferromagnetic in-plane ordering is also retained in alloy bilayers, but subsequent CuMn layers couple antiferromagnetically, the magnetic moments decreasing slightly in the deeper layers. In both cases the large local volume of the Mn atoms leads to a pronounced buckling of the surface. A detailed comparison with experiment has been performed, demonstrating the ability of LSDA+GGC calculations to describe even complex magnetic systems with high accuracy.

ACKNOWLEDGMENTS

This work has been supported by the Austrian Science Funds under Project No. P12753-PHY and by the Austrian Ministry for Science and Transport through the Center for Computational Materials Science.

[1] M. C. Cadeville and J. L. Morán-Lopez, Phys. Rep. **153**, 331 (1987).
[2] J. D. Cohen and C. P. Slichter, Phys. Rev. B **22**, 45 (1980).
[3] P. M. Marcus and V. L. Moruzzi, J. Appl. Phys. **63**, 4045 (1988).
[4] G. Fuster, N. E. Brenner, J. Callaway, J. L. Fry, Y. Z. Zhao, and D. A. Papaconstantopoulos, Phys. Rev. B **38**, 423 (1988).
[5] J. L. Fry, Y. Z. Zhao, P. C. Pattnaik, V. L. Moruzzi, and D. A. Papaconstantopoulos, J. Appl. Phys. **63**, 4060 (1988).
[6] V. L. Moruzzi, P. M. Marcus, and J. Kübler, Phys. Rev. B **39**, 6957 (1989).
[7] H. Duschanek, P. Mohn, and K. Schwarz, Physica B **161**, 139 (1989).
[8] M. Podgorny and J. Goniakowski, Phys. Rev. B **42**, 6683 (1990).
[9] J. Goniakowski and M. Podgorny, Phys. Rev. B **44**, 12 348 (1991).
[10] T. Asada, in *Interatomic Potentials and Structural Stability*, edited by K. Terakura and H. Arai, Springer Series in Solid State Sciences Vol. 114 (Springer, Berlin, 1993), p. 201.
[11] T. Asada and K. Terakura, Phys. Rev. B **47**, 15 992 (1993).
[12] V. Sliwko, P. Mohn, and K. Schwarz, J. Phys.: Condens. Matter **6**, 6557 (1994).
[13] J. Zheng-Johansson, O. Eriksson, B. Johansson, L. Fast, and R. Ahuja, Phys. Rev. B **57**, 10 989 (1998).
[14] Y. Endoh and Y. Ishikawa, J. Phys. Soc. Jpn. **30**, 1614 (1973).
[15] Y. Nishihata, M. Nakayama, N. Sano, and H. Terushi, J. Phys. Soc. Jpn. **63**, 319 (1988).
[16] W. F. Egelhoff, I. Jacob, J. M. Rudd, J. F. Cochran, and B. Heinrich, J. Vac. Sci. Technol. A **8**, 1582 (1990).
[17] B. Heinrich, A. S. Arrott, C. Liu, and S. T. Purcell, J. Vac. Sci. Technol. A **5**, 1935 (1987).
[18] D. Tian, S. C. Wu, F. Jona, and P. M. Marcus, Solid State Commun. **70**, 199 (1989).
[19] S. Andrieu, H. Fischer, A. Traverse, and M. Piecuch, Phys. Rev. B **54**, 2822 (1996).
[20] T. G. Walker and H. Hopster, Phys. Rev. B **48**, 3563 (1993).
[21] R. Q. Wu and A. J. Freeman, Phys. Rev. B **51**, 17 131 (1995).
[22] R. Q. Wu and A. J. Freeman, J. Magn. Magn. Mater. **161**, 89 (1996).
[23] D. Spišák and J. Hafner, Phys. Rev. B **55**, 8304 (1997).
[24] T. Asada and S. Blügel, Physica B **237-238**, 359 (1997).
[25] T. Flores, M. Hansen, and M. Wuttig, Surf. Sci. **279**, 251 (1992).
[26] W. L. O'Brien and B. P. Tonner, Phys. Rev. B **51**, 617 (1995).
[27] A. B. Hayden, P. Pervan, and D. P. Woodruff, J. Phys.: Condens. Matter **7**, 1139 (1995).
[28] C. Binns and C. Norris, Surf. Sci. **116**, 338 (1982).
[29] O. Rader, W. Gudat, C. Carbone, E. Vecovo, S. Blügel, R. Kläsges, W. Eberhardt, M. Wuttig, J. Redinger, and F. J. Himpsel, Phys. Rev. B **55**, 5404 (1997).
[30] M. Wuttig, Y. Gauthier, and S. Blügel, Phys. Rev. Lett. **70**, 3619 (1993).
[31] W. Kohn and L. J. Sham, Phys. Rev. **140**, A1133 (1965).
[32] J. Perdew and A. Zunger, Phys. Rev. B **23**, 5048 (1981).
[33] J. P. Perdew and Y. Wang, Phys. Rev. B **45**, 13 244 (1992).
[34] J. P. Perdew, J. A. Chevary, S. H. Vosko, K. A. Jackson, M. R. Perdersen, D. J. Singh, and C. Fiolhais, Phys. Rev. B **46**, 6671 (1992); J. P. Perdew, in *Electronic Structure of Solids 1991*, edited by P. Ziesche and H. Eschrig (Akademie Verlag, Berlin, 1991), p. 11.
[35] U. von Barth and L. Hedin, J. Phys. C **5**, 1629 (1972).
[36] J. A. White and D. M. Bird, Phys. Rev. B **50**, 4954 (1994).
[37] E. G. Moroni, G. Kresse, J. Hafner, and J. Furthmüller, Phys. Rev. B **56**, 15 629 (1997).
[38] G. Kresse and J. Hafner, Phys. Rev. B **47**, 558 (1993); Phys. Rev. B **49**, 14 251 (1994).
[39] G. Kresse and J. Furthmüller, Comput. Mater. Sci. **6**, 15 (1996).
[40] G. Kresse and J. Furthmüller, Phys. Rev. B **54**, 11 196 (1996).
[41] D. Vanderbilt, Phys. Rev. B **41**, 7892 (1990).
[42] G. Kresse and J. Hafner, J. Phys. A: Condens. Matter **6**, 8245 (1994).
[43] D. M. Wood and A. Zunger, J. Phys. A **18**, 1343 (1985).
[44] C. G. Broyden, Math. Comput. **19**, 577 (1965).
[45] P. Pulay, Chem. Phys. Lett. **73**, 393 (1980).
[46] H. J. Monkhorst and J. D. Pack, Phys. Rev. B **13**, 5188 (1976).
[47] P. E. Blöchl, O. Jepsen, and O. K. Andersen, Phys. Rev. B **49**, 16 223 (1994).
[48] A. Eichler, J. Hafner, J. Furthmüller, and G. Kresse, Surf. Sci. **346**, 300 (1996).
[49] S. G. Louie, S. Froyen, and M. L. Cohen, Phys. Rev. B **26**, 1738 (1982).
[50] N. D. Mermin, Phys. Rev. **137**, A1141 (1965).
[51] A. T. Paxton, M. Methfessel, and H. M. Polatoglou, Phys. Rev. B **41**, 8127 (1990).
[52] F. D. Murnaghan, Proc. Natl. Acad. Sci. USA **30**, 244 (1944); F. Birch, J. Geophys. Res. **57**, 227 (1952).

[53] P. Bagno, O. Jepsen, and O. Gunnarsson, Phys. Rev. B **40**, 1997 (1989).
[54] B. Barbiellini, E. G. Moroni, and T. Jarlborg, J. Phys.: Condens. Matter. **2**, 7597 (1990).
[55] J. Häglund, Phys. Rev. B **47**, 566 (1993).
[56] D. Hobbs, J. Hafner, and G. Kresse (unpublished).
[57] R. W. G. Wyckoff, *Crystal Structure* (Wiley, New York, 1963); in *Magnetic Properties of Metals*, edited by H. P. J. Wijn, Landolt-Börnstein, New Series, Group III, Vol. 19, Pt. a (Springer, Berlin, 1971) p. 17.
[58] T. J. Hics, A. R. Pepper, and J. H. Smith, J. Phys. C **1**, 1683 (1968); Y. Endoh and Y. Ishikawa, J. Phys. Soc. Jpn. **30**, 1614 (1971).
[59] Y. Tsunoda and Y. Nakai, Solid State Commun. **34**, 413 (1980).
[60] T. Oguchi and A. J. Freeman, J. Magn. Magn. Mater. **20**, 107 (1980).
[61] P. Krüger, O. Elmouhssine, C. Demangeat, and J. C. Parlebas, J. Magn. Magn. Mater. **91–93**, 156 (1996).
[62] Q. T. Jiang, P. Fenter, and T. Gustafsson, Phys. Rev. B **44**, 5773 (1991).
[63] D. Spišák and J. Hafner, J. Phys.: Condens. Matter **11**, 6359 (1999).
[64] R. Toomes, A. Theobald, R. Lindsay, T. Geißel, O. Schaff, R. Dzidszhun, D. P. Woodruff, A. M. Bradshaw, and V. Fritzsche, J. Phys.: Condens. Matter **8**, 10 231 (1996).
[65] T. Asada and S. Blügel, Physica B **237–238**, 359 (1997).
[66] J. J. Yeh and I. Lindau, At. Data Nucl. Data Tables **32**, 1 (1985).
[67] F. J. Himpsel, Phys. Rev. Lett. **67**, 2363 (1991).
[68] I. Turek, Ch. Becker, and J. Hafner, J. Phys.: Condens. Matter **4**, 7257 (1992).